J. Fluid Mech. (2023), *vol*. 961, A14, doi:10.1017/jfm.2023.248

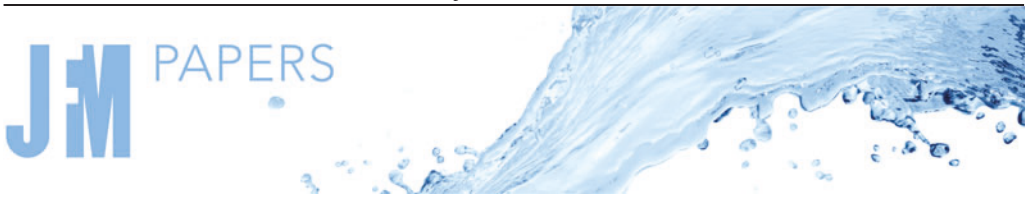

Bead-on-fibre morphology in shear-thinning flow

Chase T. Gabbard[1] **and Joshua B. Bostwick**[1,†]

[1]Department of Mechanical Engineering, Clemson University, Clemson, SC 29631, USA

(Received 18 September 2022; revised 27 January 2023; accepted 18 March 2023)

Thin-film flow down a fibre exhibits rich dynamics and is relevant to applications such as desalination, fibre coating and fog harvesting. These flows are subject to instabilities that result in dynamic bead-on-fibre patterns. We perform an experimental study of shear-thinning flow down fibres using 20 different xanthan gum solutions as our working liquid. The bead-on-fibre morphology can be oriented either symmetrically or asymmetrically on the fibre, and this depends upon the surface tension, fibre diameter and liquid rheology, as defined by the Ostwald power-law index. For highly shear-thinning liquids, it is possible for the pattern to be complex and exhibit simultaneously both asymmetric large beads and symmetric small beads in the isolated and convective flow regimes. We quantify the transition between flow regimes and bead dynamics for the asymmetric morphology, and compare with Newtonian flow, as it depends upon the experimental parameters. Finally, the dimensionless bead frequency is shown to scale with the Bond number for all of our experimental data (symmetric and asymmetric).

Key words: thin films, absolute/convective instability

1. Introduction

Thin-film flows on fibres are susceptible to shape-change instabilities that produce bead-on-fibre patterns, as seen in gas absorption (Chinju, Uchiyama & Mori 2000; Uchiyama *et al.* 2003; Grünig *et al.* 2012; Hosseini *et al.* 2014), heat exchange (Zeng *et al.* 2017; Zeng, Sadeghpour & Ju 2018), microfluidic (Gilet, Terwagne & Vandewalle 2009), moisture-capturing (Labbé & Duprat 2019; Nguyen *et al.* 2021; Moncuquet *et al.* 2022), particle-capturing (Sadeghpour *et al.* 2021), desalination (Sadeghpour *et al.* 2019) and fibre-coating technologies. In fibre coating, the liquid coating solution is often shear-thinning so as to promote spreading at high shear and inhibit uneven coating

† Email address for correspondence: jbostwi@clemson.edu

while at rest. This desirable behaviour is used to ensure optimal pigment orientation in waterborne automotive base coats (Bühne, Woocker & Linzmaier 2009; Lin, Schmelter & Hintze-Bruening 2021), for quality control in inverse dip coating of optical fibres (Brasse *et al.* 2011), and to assist in applying antibacterial nanocomposite coatings (Tang *et al.* 2016) to fibre-shaped objects such as straws and toothbrush bristles to protect against disease transmission. These various applications and the benefits of shear-thinning behaviour motivate us to explore how shear-thinning affects flow morphology in thin-film flow down a fibre. We are interested in quantifying experimentally the morphology and dynamics of bead-on-fibre patterns in thin-film flow of a shear-thinning liquid.

Early experiments on axisymmetric fibre coating focused on fibre withdrawal from a liquid bath and revealed the emergence of undesired bead-on-fibre patterns (Quéré 1999; Shen *et al.* 2002). Kliakhandler, Davis & Bankoff (2001) classified these patterns on a vertically hung fibre into three primary regimes: (i) isolated, (ii) Plateau–Rayleigh, and (iii) convective. The isolated and Plateau–Rayleigh regimes have equispaced primary beads and form steady patterns. The thin film connecting the primary beads destabilizes into smaller, secondary beads in the isolated regime, but remains uniform in the Plateau–Rayleigh regime. In the convective regime, increased inertia drives coalescence between primary beads, resulting in more complex dynamics. Convective patterns are not equispaced; however, Duprat *et al.* (2009*a*, 2011) showed that neighbouring beads can interact and form natural and forced bound states with preferential bead spacings. From a stability perspective, the steady patterns in the isolated and Plateau–Rayleigh regimes result from absolutely unstable base flows, while the convective patterns result from convectively unstable base flows (Duprat *et al.* 2007). More recently, researchers have been interested in the influence of nozzle geometry (Sadeghpour, Zeng & Ju 2017; Ji *et al.* 2020), fibre shape (Xie *et al.* 2021), fluid properties (Smolka, North & Guerra 2008; Gabbard & Bostwick 2021*b*) and slip (Haefner *et al.* 2015) on bead-on-fibre patterns.

Several models have been proposed to explain the physics governing bead-on-fibre formation. Kalliadasis & Chang (1994) considered solitary wave solutions and determined the minimal thickness h_c for pulses to grow into drops. Chang & Demekhin (1999) studied subcritical ($h < h_c$) and supercritical ($h > h_c$) films, and found that growing pulses can consume smaller, slower pulses, forming 'coalescence cascades'. An evolution equation for the interface was derived by Craster & Matar (2006) using the long-wavelength approximation and provided good predictions for the shape and speed of drops flowing down a fibre. More recently, models have considered streamwise viscous diffusion (Ruyer-Quil *et al.* 2009), slip-enhanced drop formation (Halpern & Wei 2017), disjoining pressure (Ji *et al.* 2019) and thermal gradients (Khanum & Tiwari 2020; Ji *et al.* 2021).

The literature of thin-film flow of complex fluids down fibres is comparatively sparse compared to that of Newtonian fluids. Complex fluids exhibit a shear-dependent viscosity or elasticity, or have multiple constituents and produce new behaviours of practical importance. For example, Tadmor & Bird (1974) showed that a negative second normal stress has a centring effect during wire-coating. Boulogne, Pauchard & Giorgiutti-Dauphiné (2012) performed experiments on shear-thinning and elastic polymer solutions flowing down a fibre, and derived a dispersion relation for shear-thinning flow down a fibre, with which they compare predicted to measured growth rates. Later, Boulogne *et al.* (2013) showed that worm-like micelle solutions can suppress the Plateau–Rayleigh instability by forming shear-induced structures. Pradas *et al.* (2014) expanded the study of non-Newtonian flow down a fibre by considering shear-thinning and shear-thickening behaviour of 'large' and 'fast' solitary waves. In each of these studies

of shear-dependant liquids, the resulting flow instability was symmetric about the fibre; Boulogne *et al.* (2012) did briefly mention observing asymmetric patterns, but these were not analysed further.

Asymmetric configurations have been observed previously in liquid threads and bead-on-fibre structures. For example, liquid jets have unstable asymmetric modes below a critical Weber number We_c (Yang 1992), and static droplets on a fibre can have asymmetric ('clamshell') profiles that depend upon the contact angle and volume (Carroll 1984, 1986; McHale, Newton & Carroll 2001; McHale & Newton 2002; Chou *et al.* 2011). Recently, we observed asymmetric morphologies in Newtonian flow down a fibre using high-surface-tension glycerol–water mixtures, with the azimuthal symmetry depending upon the surface tension and fibre diameter, and the bead properties following scaling laws much different to the corresponding symmetric patterns (Gabbard & Bostwick 2021*a*). The asymmetric morphology results in azimuthally asymmetric bead profiles like the 'clamshell' profile observed for static beads on a fibre; however, they are also axial asymmetric, resulting in a wide range of shapes. Eghbali *et al.* (2022) performed experiments on highly viscous Newtonian flow down a fibre, and observed two asymmetric modes: pearl and whirl. They altered the initial eccentricity of the liquid about the fibre, showing that the morphology depends on the Bond number Bo and eccentricity, and rationalized these observations using an energy analysis that showed that shear at the liquid–gas interface can sustain the whirling mode instability. Non-Newtonian liquids are ubiquitous in practice, e.g. most common paints are highly shear-thinning (Armelin *et al.* 2006). Specifically, shear-thinning behaviour is tailored easily by varying polymer concentrations, and this has been shown to enhance heat transfer in several systems (Gingrich, Cho & Shyy 1992; Ebrahimi *et al.* 2017). Despite this relevance, the literature on shear-thinning flow on fibres is sparse and has been focused primarily on axisymmetric flows. Interestingly, non-Newtonian rheology has been shown to induce asymmetric flow in microfluidic systems (Haward, Hopkins & Shen 2020). Thus we are motivated to explore how shear-thinning behaviours affect the bead properties (morphology and dynamics) in thin-film flow on fibres.

We begin this paper by describing our experiment, including the preparation of the polymer solutions and characterization of their rheology, the experimental protocol, and data analysis techniques, in § 2. We present our results in § 3, focusing on how shear thinning affects the bead morphology (§ 3.1), transition between flow regimes (§ 3.2) and bead dynamics (§ 3.3), contrasting with the Newtonian case studied previously. In § 3.4, we show that all of our data can be collapsed using appropriate scalings. In § 4, we propose a physical reason for how shear-thinning produces asymmetric morphologies. Finally, we make some concluding remarks in § 5, and identify several open questions on shear-thinning flow down a fibre.

2. Experiment

Experiments were performed by flowing shear-thinning xanthan gum (XG) solution down a fibre using the set-up shown in figure 1(*a*). An NE-1000 syringe pump applied the polymer solution onto a smooth nylon fibre of diameter D_f and length 700 mm through a circular stainless steel nozzle (1.2 mm diameter) at a constant flow rate Q. The nozzle was orthogonal to the fibre, which was vertically aligned using a free-hanging weight, pulled taut, and pinned at top and bottom. The flow rate was in the range $Q = 1$–310 ml h^{-1}, and the fibre diameter in $D_f = 0.1$–0.6 mm.

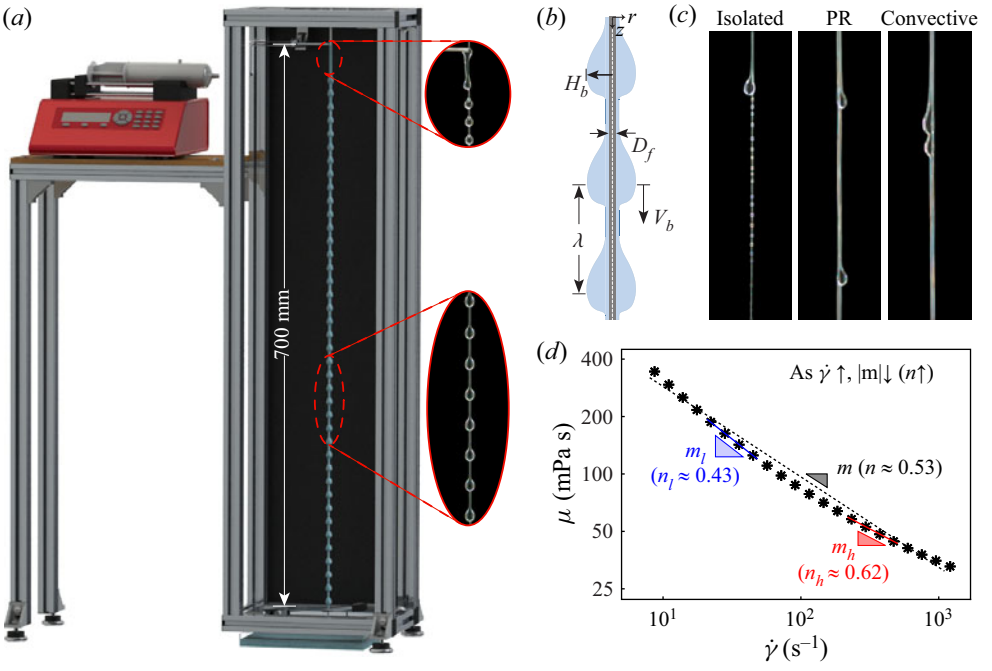

Figure 1. (*a*) Experimental set-up. (*b*) Sketch of a bead-on-fibre morphology defining the bead height H_b, fibre diameter D_f, bead spacing λ, and bead velocity V_b. (*c*) Bead-on-fibre patterns belong to the isolated, Plateau–Rayleigh (PR) or convective regimes. (*d*) Viscosity μ against shear rate $\dot{\gamma}$ for a typical 2500 ppm xanthan gum (XG) solution overlaid by a best fit to the power-law model for the full shear rate range (dashed black line), a high shear rate range (solid red line), and a low shear rate range (solid blue line). For all XG solutions, the estimated power-law exponent increased with shear rate such that $n_l < n < n_h$ (i.e. the degree of shear-thinning decreased as $\dot{\gamma}$ increased).

Three beading patterns were observed: (i) isolated, (ii) Plateau–Rayleigh, and (iii) convective, as shown in figure 1(*c*). These are consistent with those observed for Newtonian flow down a fibre (Kliakhandler *et al.* 2001). In all experiments, the regime transitioned from isolated to Plateau–Rayleigh to convective as the flow rate Q was increased. The bead dynamics were recorded 550 mm down the fibre (to ensure fully developed flow) at either 500 fps or 1000 fps using a Phantom VEO 410L high-speed camera. ImageJ was used for image processing to quantify the bead height H_b (measured from the fibre centreline), velocity V_b, and spacing λ, as shown in figure 1(*b*). The bead frequency is also of practical importance, and we calculated it as $f = V_b/\lambda$.

2.1. *Rheology of XG solutions*

Xanthan gum solutions were prepared by dissolving XG ($M_w \approx 2$ MDa, Tokyo Chemical Industry, Tokyo, Japan) of concentrations 200–2500 ppm in a glycerol–water mixture solvent; two glycerol concentrations (60 %w and 80 %w) were used to explore different solvent viscosities. The solution was covered and placed on a magnetic stirrer for 24 h. Tween-20 (T20) surfactant (Sigma–Aldrich; CAS: 9005-64-5) was then added to the solution in concentrations 0.02–4 %w. We note that Dacus *et al.* (2022) observed that Tween-20 can affect the rheology of XG solutions in water; however, we observe a negligible effect on the rheology of our glycerol–water solvents, likely due to their high

Label	Glycerol/water (%)	ϕ (ppm)	T20 (%)	NaCl (%)	σ (mN m^{-1})	β (mPa s^n)	n
1	60/40	2500	4	0	33	814.5	0.53
2	60/40	2000	4	0	33	635.4	0.55
3	60/40	2000	0.1	0	39.6	665.4	0.54
4	60/40	2000	0.02	0	48.4	678.7	0.52
5	60/40	2000	0	0	67.3	601.1	0.53
6	60/40	1500	4	0	32.8	474.4	0.57
7	60/40	700	4	0	31.1	180.1	0.69
8	60/40	600	4	0	32	147.7	0.7
9	60/40	500	4	0	31.2	138.2	0.71
10	60/40	450	4	0	31.3	127.3	0.73
11	60/40	400	4	0	32.6	101.6	0.75
12	60/40	300	4	0	31.8	78.6	0.77
13	60/40	200	4	0	31.8	53.2	0.82
14	80/20	500	4	4	32.3	914.4	0.93
15	80/20	500	4	3	31.8	840.7	0.91
16	80/20	500	4	2	31.5	564.4	0.89
17	80/20	500	4	1	31.4	449.2	0.87
18	80/20	500	4	0.8	31	237.6	0.86
19	80/20	500	4	0.5	30.7	273.2	0.82
20	80/20	500	4	0	30.6	294.4	0.79

Table 1. Liquid properties for XG solutions tested: surface tension σ, and the consistency coefficient β and power-law index n for the Ostwald power-law rheology model.

glycerol concentration (cf. solutions 2–5 in table 1). Additionally, we note that the presence of a surfactant can induce Marangoni effects. However, nearly all of our solutions have surfactant concentration larger than the critical micelle concentration, suggesting the absence of Marangoni effects, with the potential exception of solutions 3 and 4 (cf. table 1). Finally, sodium chloride (NaCl) was added in concentrations 0–5 %w to weaken the shear-thinning behaviour (Wyatt & Liberatore 2009). The solution was mixed until no streaks or clumps were visible, and then bottled and stored at 2 °C. The solutions were removed from the cooled environment and allowed to warm to room temperature (≈21 °C) before we measured the rheology or performed experiments.

We used 20 different XG solutions in our experiments, with liquid properties given in table 1. The surface tension σ and density ρ were measured using an Attension Sigma 702 tensiometer with Wilhelmy plate and density probe, respectively. Here, the surface tension was in the range 30.64–67.32 mNm^{-1}, and the density in 1135.4–1244.2 kg m^{-3}. The viscosity μ was measured against shear rate $\dot{\gamma}$ using an Anton Paar MCR 302 rheometer with a cone geometry over a range of shear rates 10–1000 s^{-1} that encompasses the typical range for thin-film flow down a fibre (Duprat, Ruyer-Quil & Giorgiutti-Dauphiné 2009*b*; Boulogne *et al.* 2012). Figure 1(*d*) shows a typical viscosity curve $\mu(\dot{\gamma})$ together with a fit to the Ostwald power-law model $\mu = \beta\dot{\gamma}^{n-1}$ (black dashed line), where β is the consistency coefficient (a measure of the solvent viscosity), and n is the power-law index, a measure of the shear-thinning behaviour with limiting case $n = 1$ for a Newtonian liquid. We note that the local estimate of n, calculated about a specific shear rate $\dot{\gamma}$, varies greatly from the global estimate. For example, the blue and red lines in figure 1(*d*) show the slope of the viscosity curve at low (blue) and high (red) values of $\dot{\gamma}$; n varies greatly in this range ($0.43 \leq n \leq 0.62$).

To best delineate the role of shear-thinning on the bead properties, we estimate n and μ for each experiment. We do this at steady state, assuming that the low-viscosity regions control the bead dynamics. This occurs along the fibre–liquid interface, and we can estimate the shear rate there as $\dot{\gamma} \approx V_b/H_b$. The rheology ($n$ and μ) can then be determined through interpolation of the viscosity curve. Herein, when we report our data, it will be with respect to this viscosity.

3. Results

This section describes our experimental results and shows how the bead symmetry depends upon the rheology and fibre diameter. We quantify the conditions under which asymmetric morphologies transition (i) from the isolated to the Plateau–Rayleigh regime, and (ii) from the Plateau–Rayleigh to the convective regime. For patterns that result from an absolutely unstable base flow (isolated and Plateau–Rayleigh regimes), we determine the bead dynamics through the bead velocity V_b, spacing λ, and frequency f. Finally, we attempt to scale our experimental data for both symmetric and asymmetric morphologies.

3.1. *Bead symmetry*

Figure 2 plots the bead morphology (blue circles for symmetric, red triangles for asymmetric) as it depends upon n and D_f for all experiments where $\sigma \leq 33.03$ mN m^{-1}; the insets show each morphology. Here, the bead morphology is determined from the Plateau–Rayleigh regime – an important distinction on which we will expand shortly. Two trends are observed: (i) for fixed D_f, decreasing n (increasing shear-thinning) leads to asymmetry, and (ii) for fixed n, increasing D_f leads to asymmetry, both of which show that shear-thinning affects bead morphology. The critical power-law index n_c for transition between the two morphologies is a monotonically increasing function of D_f. This is consistent with our prior results for Newtonian fluids (Gabbard & Bostwick 2021*a*). Interestingly, our prior experiments on Newtonian (glycerol) liquids with $\sigma \approx 30$ mNm^{-1} exhibited an asymmetric morphology for our largest fibres ($D_f \geq 0.5$ mm), whereas our XG solutions with similar surface tension σ are symmetric as $n \to 1$ for $D_f = 0.6$ mm. Slight discrepancies are expected when comparing two different mixtures close to a transition point. Still, the literature on static beads on fibres may provide a simple reason why this mismatch can occur. McHale *et al.* (2001) showed that the morphology of a static Newtonian bead on a fibre depends upon the drop volume V and D_f. In our experiments, we set D_f, but V is difficult to measure as this requires one to (i) capture a complex bead geometry at high resolution, and (ii) determine a consistent method for distinguishing the volume of liquid associated with the bead from that associated with the thin film on the fibre. This is compounded by the fact that the bead can rotate about the fibre. Here, we use glycerol–water mixtures as the solvent for our polymer solutions, which are the same as used in our Newtonian experiments (Gabbard & Bostwick 2021*a*); however, adding polymer may slightly affect V, leading to morphology differences near the transition point.

Qualitative evidence suggests that the mechanism responsible for the asymmetric morphology in shear-thinning flow is different from that in Newtonian flow. Figure 3(*a*) shows two examples of beading patterns with asymmetric morphology in the isolated regime for a Newtonian liquid (glycerol) and a shear-thinning liquid (XG). Here, the largest bead flows down the fibre, consuming the smaller, static beads below it. The large bead is asymmetric in both cases; however, the smaller, static beads are asymmetric only for Newtonian flow. The smaller, shear-thinning beads remain symmetric without flow

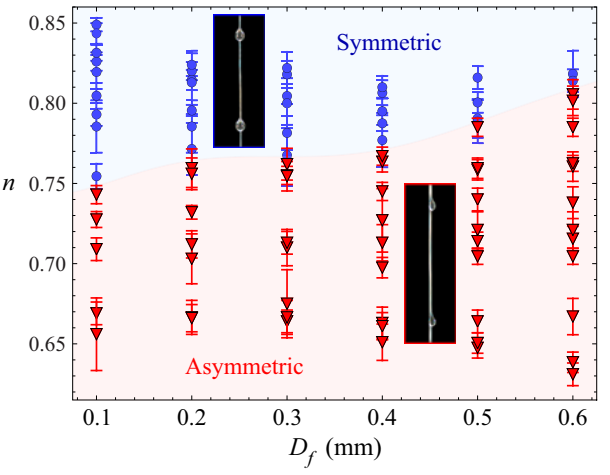

Figure 2. Phase diagram of the bead symmetry as it depends upon the power-law index n and fibre diameter D_f for all experiments with $\sigma \leq 33.03$ mN m^{-1}. Inset images show typical symmetric (blue) and asymmetric (red) morphologies.

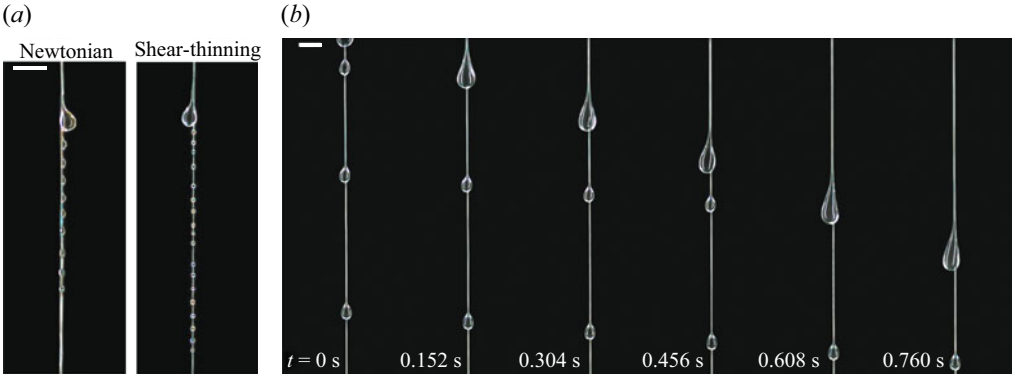

Figure 3. (*a*) Complex bead morphology revealed by contrasting Newtonian and shear-thinning flow in the isolated regime, noting that the large beads are asymmetric for both cases, but the smaller beads are asymmetric for Newtonian flow and symmetric for shear-thinning flow due to the absence of shear. (*b*) An image sequence of a convective bead pattern showing the large bead transition from symmetric to asymmetric as it consumes smaller beads, causing it to gain mass, increase speed, and produce the necessary internal shear for symmetry transition. Note that the white scale bars have a width of 4 mm.

since no shear is produced in the liquid. These observations hold for all Newtonian and shear-thinning experiments in the isolated flow regime.

A similar phenomenon occurs in the convective regime; however, in this case, the smaller beads are no longer static. Figure 3(*b*) shows an image sequence of a large, shear-thinning bead that transitions from symmetric to asymmetric as it flows down the fibre consuming smaller beads. Convective interactions allow the large bead to grow and speed up. After consuming the top, smaller bead in the first image ($t = 0$ s), the large bead begins to transition to an asymmetric morphology, with subsequent images depicting this process. Similar to figure 3(*a*), the smaller beads are symmetric but are now dynamic and flowing down the fibre at a constant velocity. In both cases, the smaller beads remain symmetric because there is not enough shear to change their morphology, while the larger

beads have accumulated enough mass to make this transition occur. Both of these examples illustrate that the mechanism for the formation of an asymmetric bead morphology in shear-thinning liquids is shear-dependent, and unique from that observed for Newtonian liquids. Earlier, we mentioned that we characterized the morphology of each experiment in the Plateau–Rayleigh regime, and these observations illustrate why: a regime transition increases the bead size, which increases the shear inside the liquid, potentially altering the morphology classification. In the Plateau–Rayleigh regime, the beads have uniform size and speed, and none of the aforementioned complexities occurs.

3.2. *Regime transition*

Three primary flow regimes are observed for both symmetric and asymmetric morphologies: (i) isolated, (ii) Plateau–Rayleigh, and (iii) convective. Flows in the isolated and Plateau–Rayleigh regimes result from an absolute instability and have equispaced beads flowing down the fibre with a constant velocity. The beads are connected by a thin, uniform film in the Plateau–Rayleigh regime, whereas in the isolated regime, the thin film destabilizes into a string of smaller static beads. The convective regime emerges at higher Q and larger D_f where the base flow is convectively unstable, leading to interactions between beads. Here, we focus on classifying the transition points between (i) the isolated and Plateau–Rayleigh regimes, and (ii) the Plateau–Rayleigh (absolute instability) and convective (convective instability) regimes for the asymmetric morphology, as they depend on the power-law index n.

The transition between the isolated and Plateau–Rayleigh regimes is important in coating processes, as the uniform film between beads remains 'wet' in the Plateau–Rayleigh regime, but breaks up into secondary beads in the isolated regime, resulting in 'dry' sections. Figure 4(*a*) plots the transition flow rate $Q_{Iso/PR}$ between the isolated and Plateau–Rayleigh regimes against n for $D_f = 0.4$ mm, as it depends upon the viscosity. Here, $Q_{Iso/PR}$ increases with n, and in the $n = 1$ limit, $Q_{Iso/PR}$ decreases with increasing viscosity μ. Since the viscosity μ of the shear-thinning solutions is always smaller than that of the $n \to 1$ limit, $Q_{Iso/PR}$ increases nonlinearly with n. Figure 4(*b*) plots the bead spacing $\lambda_{Iso/PR}$ at the transition between the isolated and Plateau–Rayleigh regimes against power-law index n for $D_f = 0.4$ mm. Here, $\lambda_{Iso/PR}$ decreases as n increases, and this result follows intuition. The transition from the isolated to Plateau–Rayleigh regimes occurs when the thin film between primary beads does not have enough time to destabilize into a string of smaller, secondary beads. For Newtonian flow, the viscosity μ is the same in the beads and the thin film connecting them. In contrast, for shear-thinning flow, the liquid in the thin film has a much lower shear rate (higher viscosity) than in the primary bead region near the fibre. This increased viscosity delays secondary breakup, allowing the thin film to persist (equivalently, Plateau–Rayleigh regime) at lower flow rates Q and for larger λ than Newtonian flow.

Next, we focus on the transition between the Plateau–Rayleigh regime, which results from an absolute instability (Abs), and the convective regime, a result of a convective instability (Conv). In the Plateau–Rayleigh regime, as Q increases, the interfacial area available for heat and mass transfer increases. However, increasing Q also leads to convective patterns, which exhibit less consistent bead dynamics that yield no further heat or mass transfer benefits. Thus this transition is practically important because it is typically where optimal heat and mass transfer rates occur. Figure 5(*a*) plots the transition flow rate $Q_{Abs/Conv}$ between the Plateau–Rayleigh and convective regimes against n for $D_f = 0.4$ mm. Similar to the transition between the isolated and Plateau–Rayleigh

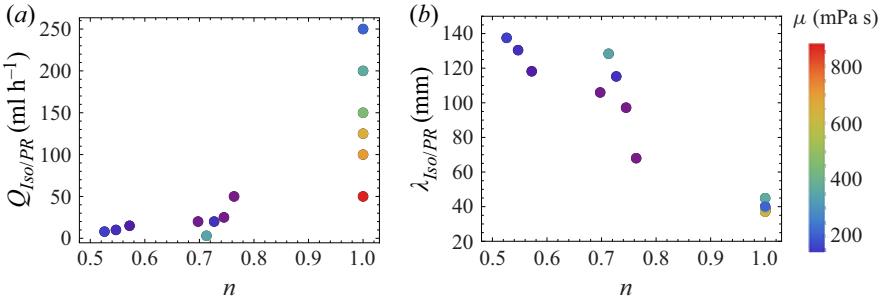

Figure 4. Isolated to Plateau–Rayleigh regime transition by plotting (*a*) the flow rate $Q_{Iso/PR}$ and (*b*) the bead spacing $\lambda_{Iso/PR}$ against power-law index n for a fixed fibre diameter $D_f = 0.4$ mm. The marker colour indicates the characteristic viscosity μ.

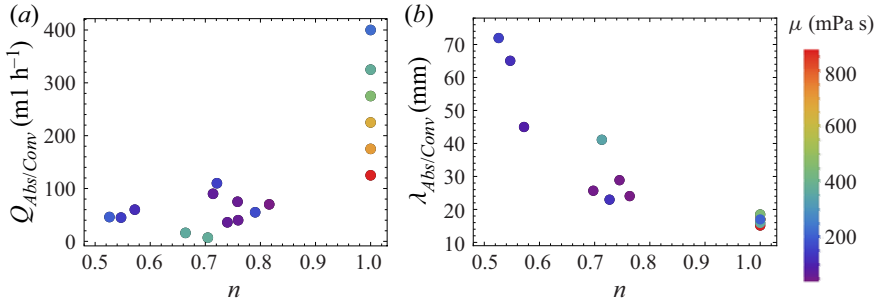

Figure 5. Plateau–Rayleigh (Abs) to convective (Conv) regime transition by plotting (*a*) the flow rate $Q_{Abs/Conv}$ and (*b*) the bead spacing $\lambda_{Abs/Conv}$ against power-law index n for a fixed fibre diameter $D_f = 0.4$ mm. The marker colour indicates the characteristic viscosity μ.

regimes, increasing n increases $Q_{Abs/Conv}$. Figure 5(*b*) plots the bead spacing $\lambda_{Abs/Conv}$ at the transition between the Plateau–Rayleigh and convective regimes against n for $D_f = 0.4$ mm, showing that $\lambda_{Abs/Conv}$ decreases as n increases, approaching a constant bead spacing at $n = 1$. Two beneficial properties of shear-thinning flow are observed: (i) the maximum bead frequency, which occurs just before $Q_{Abs/Conv}$, is obtained at lower flow rates Q than Newtonian liquids; and (ii) the bead spacing $\lambda_{Abs/Conv}$ can be adjusted through the power-law index n, whereas for Newtonian liquids it is approximately constant and independent of viscosity.

3.3. *Bead dynamics*

The bead dynamics is described by the bead velocity V_b, spacing λ, and frequency f. Previous studies have explored the dynamics of the symmetric morphology (Boulogne *et al.* 2012), thus we focus on the asymmetric morphology, presenting data only for absolutely unstable base flows, i.e. isolated and Plateau–Rayleigh regimes. We focus on either (i) all absolutely unstable flows or (ii) the absolute–convective transition point. The absolutely unstable data reflect robust bead dynamics (no convective bead interactions), desirable for most applications, and the absolute–convective transition points trace the boundary where these desirable patterns break down.

Shear-thinning affects the bead dynamics of asymmetric morphologies, which we quantify using three highly shear-thinning $n \leq 0.6$ solutions (solutions 1, 2 and 5 in

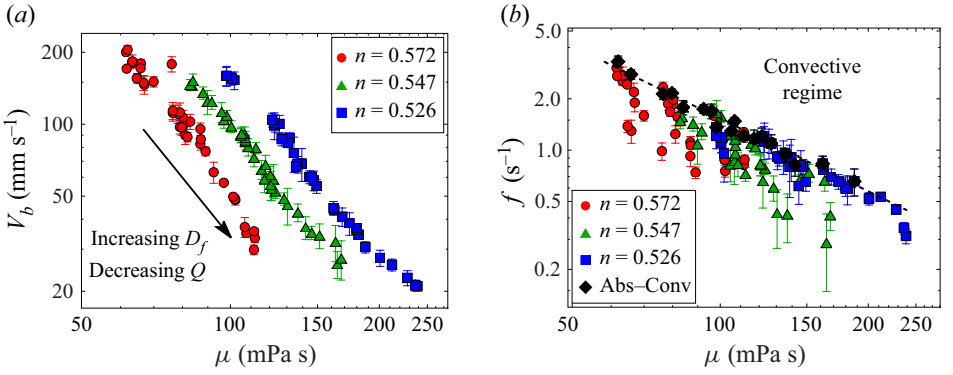

Figure 6. Bead dynamics for absolutely unstable flows, plotting (*a*) the bead velocity V_b and (*b*) the frequency f against characteristic viscosity μ as it depends upon the power-law index n for all highly shear-thinning experiments ($n < 0.6$).

table 1) to ensure that the morphology is asymmetric for all solution–fibre combinations. Figure 6(*a*) plots the bead velocity V_b against the characteristic viscosity μ as it depends upon n for all absolutely unstable flows. The data for each solution follow a similar trend. For fixed μ, increased shear-thinning tends to increase the bead velocity. Increasing the fibre diameter D_f and decreasing the flow rate Q reduce the bead velocity, the same as for Newtonian flow. Figure 6(*b*) plots the bead frequency f against viscosity μ as it depends upon n for all absolutely unstable flow. The absolute–convective transition point for each experiment is shown as a black diamond. Similar to Newtonian flow, the maximum frequency f for each experiment occurs just before the transition from absolute to convective instability, and follows a power-law trend for highly shear-thinning solutions.

Figure 7(*a*) plots bead velocity V_b against viscosity μ as it depends upon surface tension σ for all absolutely unstable data. Here, the data follow a similar trend, suggesting that the surface tension σ plays a minimal role in determining V_b compared to the viscosity μ and power-law index n. Figure 7(*b*) plots bead spacing λ against fibre diameter D_f as it depends upon surface tension σ at the absolute–convective transition point, showing that σ has a minimal effect on λ for D_f, but significantly increases λ for small D_f. This observation is expected since for vanishingly small D_f, we should recover the canonical Plateau–Rayleigh instability, which is capillary-driven. Thus σ plays a role in setting the bead dynamics by increasing λ (and thus decreasing f) when $D_f \leq 0.4$ mm. Additionally, σ alters the bead profile. Figure 7(*c*) plots bead height H_b at the absolute–convective transition point against D_f as it depends upon σ, showing that H_b increases with σ. Interestingly, while σ plays a diminishing role in determining λ as $D_f \to 0$, σ affects H_b for all D_f.

The bead frequency $f = V_b/\lambda$ is an important property in heat and mass transfer applications. Until now, we have focused primarily on the bead properties for the asymmetric morphology. Here, we show that the bead properties for the asymmetric morphology seen in highly shear-thinning ($n \leq 0.6$) flow are similar to those in the symmetric morphology observed in weakly shear-thinning ($n \geq 0.8$) flow. Figure 8 plots the frequency f against flow rate Q for all absolutely unstable asymmetric (red triangle) and symmetric (blue circle) data, showing that the data follow a similar linear trend regardless of morphology, with slope $\approx 1/50$. In our previous work, we showed that the bead frequency for the asymmetric morphology of Newtonian liquids followed a singular linear trend, but that for the symmetric morphology it did not (Gabbard & Bostwick 2021*a*).

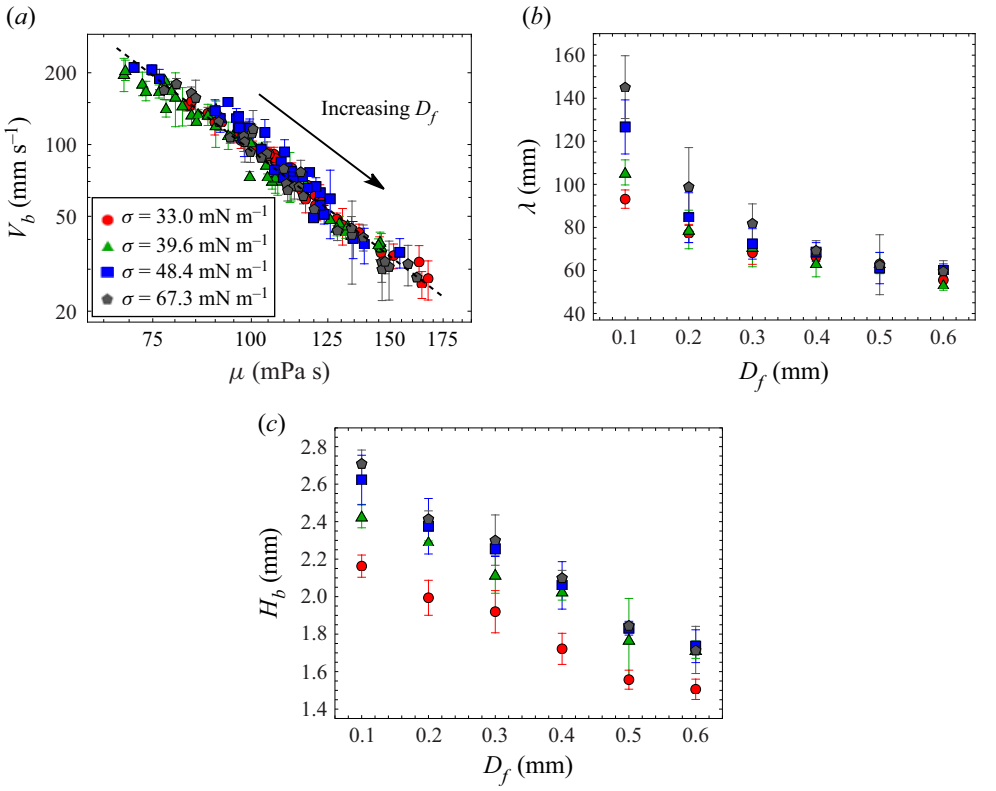

Figure 7. (*a*) Bead velocity V_b against viscosity μ as it depends upon the surface tension σ for all absolutely unstable data. (*b*) Bead spacing λ and (*c*) Bead height H_b at the absolute–convective transition point against fibre diameter D_f as it depends upon the surface tension σ for 2000 ppm XG solutions.

In contrast to Newtonian flow, shear-thinning flows reveal a symmetry-independent trend that can be used to estimate frequency f for any flow rate Q, independent of D_f, σ or morphology. This is a useful design tool for applications where these properties vary greatly or are not well known. Coupling this with our earlier observation that the maximum frequency f occurs at the absolute–convective transition point, bead-on-fibre patterns can be designed to be absolutely unstable with a desired frequency f for a known n simply by selecting the proper flow rate Q.

3.4. *Scaling the data*

We now attempt to collapse our data upon scaling, focusing on the bead frequency. We begin by using the analysis of Boulogne *et al.* (2012), who used normal mode perturbations of the form $\exp(\mathrm{i}(kz - \omega(k)t))$ to derive a dispersion relation $\omega(k)$ for axisymmetric shear-thinning flow down a fibre using the planar approximation $h \ll R_f$, where h and R_f are the initial film thickness and fibre radius. They calculated the instability growth rate Ω as the maximum of $\mathrm{Im}(\omega(k))$:

$$\Omega = \frac{q_0 \sigma}{4n\rho g R_f^4}, \tag{3.1}$$

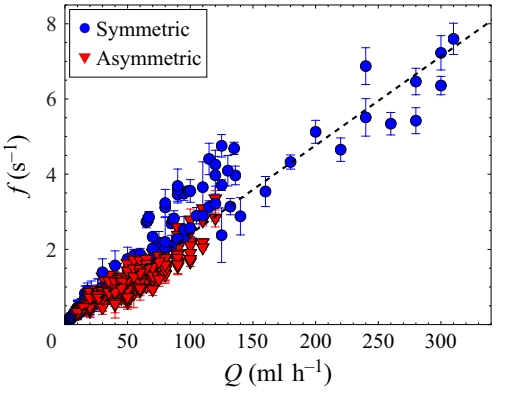

Figure 8. Frequency f against flow rate Q for all symmetric morphologies and highly shear-thinning asymmetric morphologies ($n < 0.6$).

where q_0 (in $m^2\ s^{-1}$) is the flow rate associated with the initial flat-film thickness h. We modify this analysis to account for the volumetric flow rates (in $m^3\ s^{-1}$) in our experiments: (i) we replace q_0 ($m^2\ s^{-1}$) with Q ($m^3\ s^{-1}$); and (ii) we change R_f^4 to R_f^5 to account for the additional length scale. We scale the bead frequency f with the modified growth rate Ω_{mod},

$$\frac{f}{\Omega_{mod}} = \frac{4nf\rho g R_f^5}{\sigma Q} = \tilde{f}\, Bo, \tag{3.2}$$

and define the non-dimensional frequency $\tilde{f} = 4nfR_f^3/Q$. The Bond number $Bo = \rho g R_f^2/\sigma$ appears naturally from this scaling, and accordingly we plot $\tilde{f}$ against Bo for all of our data (asymmetric and symmetric) in figure 9. The data collapse along a single trend line (black dashed line) with a power-law fit $\tilde{f} \sim Bo^{1.6}$. The Bond number Bo compares the two components of pressure acting on the drop, hydrostatic and capillary, and our scaling analysis shows that the bead dynamics is governed by the competition between the two, irrespective of n or morphology. This observation simplifies drastically our understanding of the physics governing shear-thinning flow down a fibre.

4. Discussion

Our experimental results have shown that shear-thinning can produce asymmetric morphologies, and we are interested in the mechanism responsible for this observation. Our hypothesis is that asymmetric flow emerges due to variable flow resistance about the fibre due to an initial asymmetry in the film. This idea is illustrated in the schematic diagram of figure 10, which depicts the transition from a slightly asymmetric film to a heavily asymmetric bead. Here, we illustrate the regions of maximum shear stress (minimum viscosity) by the colour intensity. In figure 10(a), an initial asymmetry causes a non-uniform shear distribution in the film that results in a gradient in the apparent viscosity about the fibre. The viscosity is lowest in the thickest portion of the film, and for sufficient Q and n can produce an azimuthal flow u_θ, as shown in figure 10(b). Once an azimuthal flow is initiated, the increased flow to the low-resistance (thickest) region further increases the viscosity gradient driving the azimuthal flow, resulting in a positive feedback loop. This process continues until the flow is heavily asymmetric and only a thin, highly

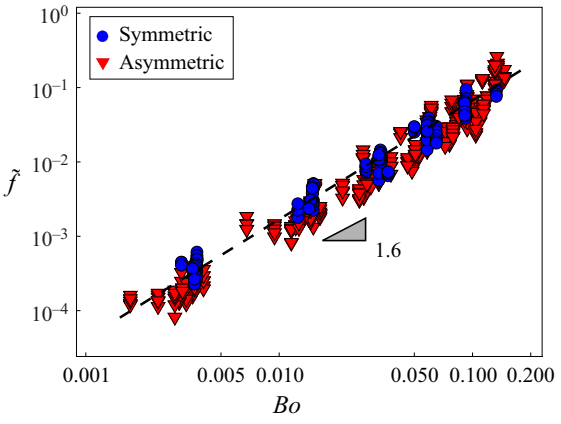

Figure 9. Dimensionless frequency $\tilde{f}$ against Bond number Bo for symmetric (blue circles) and asymmetric (red triangles) data. The data are fitted to power laws (dashed line) with associated exponent.

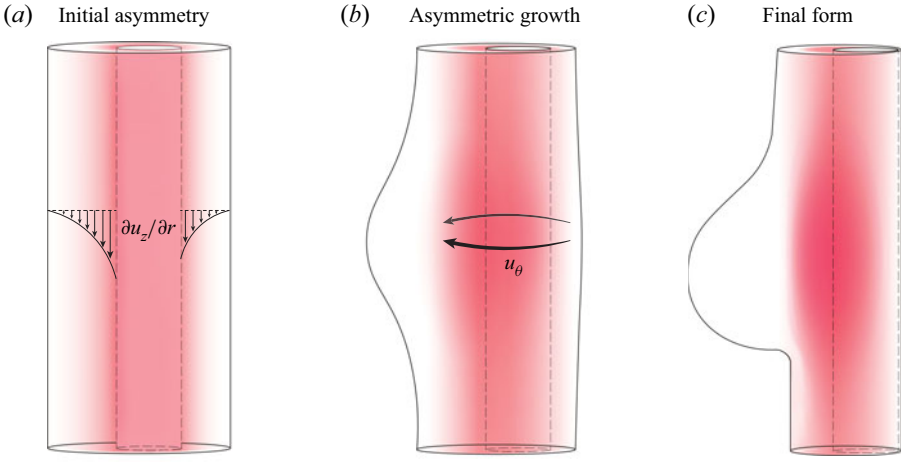

Figure 10. Schematic of the asymmetric growth of a sheath of shear-thinning fluid, where red indicates regions of high shear (low viscosity). A slightly asymmetric (a) initial profile causes a shear rate gradient about the fibre resulting in a region of low resistance (viscosity) at the liquid–fibre interface where the sheath is thickest. An azimuthal flow u_θ results, and the film destabilizes into (b) a wavy profile. Azimuthal flow towards the thickest portion of the sheath further increases the shear rate gradient, resulting in a self-reinforced process that continues until (c) a liquid bead protrudes from one side of the fibre, the opposite of a thin, low-shear film.

viscous film remains on the thin side of the fibre, as shown in figure 10(c). Our hypothesis aligns well with the observation of morphologies with fast-moving asymmetric primary beads and slow-moving symmetric secondary beads. In Appendix A, we perform a simple two-dimensional analysis that compares the shear distribution on the thinnest and thickest regions of an initially asymmetric flow, which further supports our hypothesis.

Newtonian flows also can have an azimuthal shear gradient when the film is initially asymmetric. However, in this case, the viscosity is independent of shear rate; thus asymmetry must arise from a different mechanism. Recent work by Eghbali *et al.* (2022) showed that shear along the liquid–gas interface of a Newtonian liquid can sustain asymmetric flows for thick, viscous films flowing down a fibre using an energy

balance analysis. However, the asymmetry of a Newtonian bead-on-fibre pattern remains an open topic for investigation, and the mechanism responsible for amplifying and sustaining it has yet to be determined.

5. Concluding remarks

We performed an experimental investigation of shear-thinning flow down fibres using 20 unique xanthan gum solutions to show how shear-thinning affects bead-on-fibre morphologies. Asymmetric bead morphologies were observed when either (i) shear-thinning, as quantified by the power-law index n, or (ii) fibre diameter D_f, were increased. Qualitative observations show that unlike the asymmetric morphology of Newtonian liquids (Gabbard & Bostwick 2021*a*), shear-thinning solutions can exhibit patterns containing both morphologies; small, static beads may be symmetric, while larger, faster beads are asymmetric. The asymmetric morphologies of Newtonian and shear-thinning liquids exhibit the same three flow regimes (isolated, Plateau–Rayleigh, convective), but shear-thinning significantly decreases the flow rate Q and increases the bead spacing λ at the transition points (i) between the isolated and Plateau–Rayleigh regimes, and (ii) between the Plateau–Rayleigh and convective regimes. The bead dynamics for the asymmetric morphology was explored for different n, Q and σ, and compared to the Newtonian case. The maximum bead frequency f (equivalently, minimum λ) occurs at the absolute–convective transition point, similar to the Newtonian case. The frequencies f of the symmetric and asymmetric morphologies follow a similar trend as Q increases, which was not observed for Newtonian flow. Finally, we showed that the dimensionless bead frequency $\tilde{f}$ collapses upon scaling with the Bond number Bo for all of our experimental data (asymmetric and symmetric).

Our investigation was motivated by the growing popularity of bead-on-fibre patterns for heat and mass transfer applications and fibre-coating processes that use shear-thinning paints and coating agents. Specifically, we have shown that shear-thinning reduces the transition flow rate Q between the isolated and Plateau–Rayleigh regimes. Fibre coating processes benefit from this shear-thinning effect as highly shear-thinning paints can form asymmetric bead-on-fibre patterns, which flow faster than symmetric beads, and quickly shed from the fibre, leaving behind a thin and uniform, axisymmetric coating at minimal Q. The quicker transition between the isolated and Plateau–Rayleigh regimes is also beneficial for heat and mass transfer applications where 'dry' sections of fibre reduce efficiency. Similarly, the transition point between absolute (Plateau–Rayleigh regime) and convective instability also occurs at lower Q for shear-thinning flow. Heat and mass transfer applications are optimized at this location since, as shown, the bead frequency f is maximized just before this transition; thus a lower flow rate Q is needed for this optimization. The bead geometry also affects heat and mass transfer, which we have shown to depend upon the Bond number Bo, regardless of symmetry. These examples highlight the many benefits of utilizing shear-thinning flow down a fibre.

Our experimental results provide some insight into the physics governing shear-thinning bead-on-fibre patterns; however, many questions remain. For example, in fibre-coating, the coating agent is typically shear-thinning and thixotropic. Here, we have considered explicitly shear-thinning liquids, but expect thixotropic behaviour to delay secondary destabilization, e.g. the required flow rate Q for Plateau–Rayleigh patterns. In addition, our observations show a shear-dependent mechanism for asymmetry that is different from that observed in Newtonian liquids. However, both are likely to affect shear-thinning liquids. Determining the boundary between the mechanisms is a valuable next step and will require

a better understanding of the mechanism resulting in asymmetric patterns in Newtonian flow down a fibre. Finally, the theory of absolute and convective instability has not been applied to shear-thinning flow down a fibre despite its practical relevance in application. Thin-film flow down a fibre exhibits a rich physics that is highly relevant to applications, and we have shown how shear-thinning behaviour expands upon these complexities, thus opening new avenues for exploration.

Funding. J.B.B. acknowledges support from NSF grant CMMI-1935590.

Declaration of interests. The authors report no conflict of interest.

Author ORCIDs.
Joshua B. Bostwick https://orcid.org/0000-0001-7573-2108.

Appendix A. Two-dimensional analysis of the asymmetry mechanism

We can semi-quantify our qualitative hypothesis for the mechanism of asymmetry. We begin by following the work of Boulogne *et al.* (2012) in writing the stress balance for axisymmetric shear-thinning flow down a fibre:

$$\frac{1}{r}\frac{\partial\left(r\sigma_{rz}\right)}{\partial r}=\frac{\partial p}{\partial z}-\frac{\partial\sigma_{rr}}{\partial z}-\rho g, \tag{A1}$$

where $\boldsymbol{\sigma}$ is the stress tensor, p is the pressure, ρ is the fluid density, and g is gravitational acceleration. We assume no-slip at the fibre $u_z(r=R_f)=0$ and no-shear at the liquid–gas interface $(\partial u_z/\partial r)(r=R_f+h)=0$, and introduce the following dimensionless variables: $\tilde{r}=(r-R_f)/R_f$, $\tilde{h}=h/R_f$ and $\tilde{u}_z=u_z/V$, where $V=R_f((\rho g R_f)/\beta)^{1/n}$. The shear rate can be written as

$$\dot{\gamma}=\frac{\partial\tilde{u}_z}{\partial r}=\left(\frac{1}{1+\tilde{r}}\left(\tilde{h}\left(1+\frac{\tilde{h}}{2}\right)-\tilde{r}\left(1+\frac{\tilde{r}}{2}\right)\right)\right)^{1/n}, \tag{A2}$$

and the flow rate $\tilde{q}$ is determined by integrating the liquid velocity over the film height:

$$\tilde{q}=\int_0^{\tilde{h}}\tilde{u}_z(\tilde{r}+1)\,\mathrm{d}\tilde{r}. \tag{A3}$$

For a given flow rate $\tilde{q}$, the film thickness $\tilde{h}$ can be determined from (A3) using an iterative bisection method. Then the shear rate distribution can be determined numerically from (A2).

Figure 11(*a*) illustrates flat-film flow down a fibre with two thicknesses $h_1>h_2$ and their associated shear rate profiles. The thicker film results in a higher shear rate at $r=R_f$, illustrating that the flow is least viscous where the film is thickest. Lower flow resistance along the thicker portion of the liquid sheath increases flow through that location, increasing the thickness and amplifying the initially small thickness difference into a fully asymmetric pattern.

We plot the dimensionless shear rate $\tilde{\dot{\gamma}}$ against radial position $\tilde{r}$ as it depends upon n for $\tilde{q}=1$, and $\tilde{q}$ for $n=0.7$ in figures 11(*b*,*c*), respectively. In all cases, the maximum shear rate $\tilde{\dot{\gamma}}_{max}$ occurs at the liquid–fibre interface ($\tilde{r}=0$) and decreases monotonically to zero at $\tilde{r}=\tilde{h}$, as shown in the insets. The maximum shear rate increases as n decreases and $\tilde{q}$ increases. Since our experiments show that the asymmetric morphology occurs at small

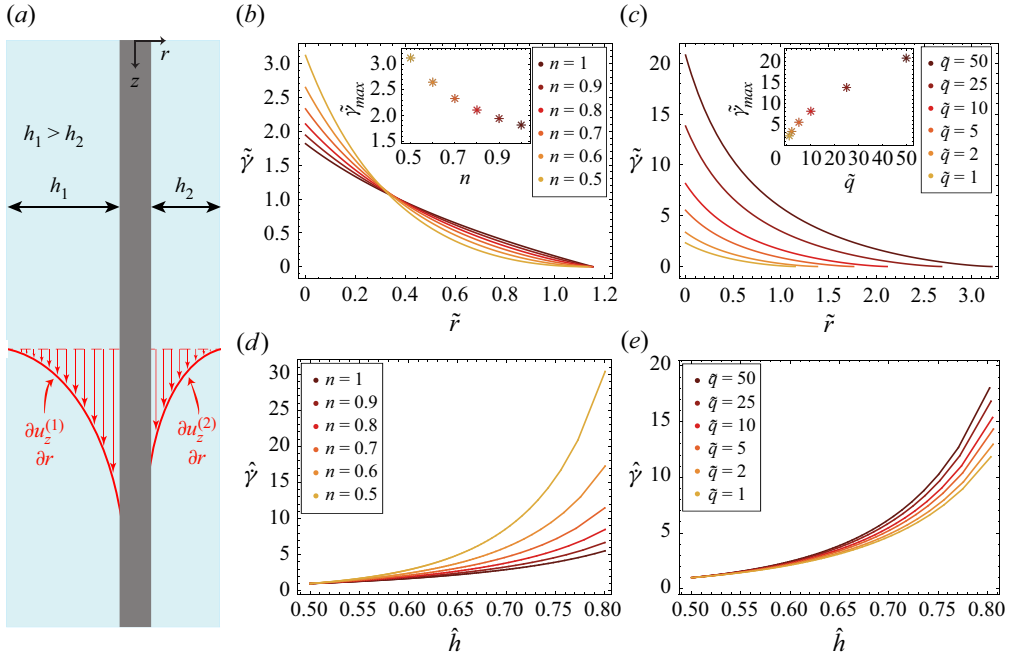

Figure 11. (*a*) Schematic of asymmetric flat-film flow down a fibre showing the shear rate profiles $\dot{\gamma} = \partial u_z/\partial r$ associated with different thicknesses, where $\dot{\gamma}_1 > \dot{\gamma}_2$ for all $R_f \leq r < R_f + h$ since $h_1 > h_2$. Plots of dimensionless shear rate $\tilde{\dot{\gamma}}$ against dimensionless radius $\tilde{r}$ as it depends upon (*b*) power-law index n for $\tilde{q} = 1$, and (*c*) dimensionless flow rate $\tilde{q}$ for $n = 0.7$, with maximum shear rates shown as insets for each plot. Plots of shear rate ratio $\hat{\dot{\gamma}} = \tilde{\dot{\gamma}}_1/\tilde{\dot{\gamma}}_2$ against thickness ratio (asymmetry) $\hat{h} = h_1/(h_1 + h_2)$, as it depends upon (*d*) power-law index n for $\tilde{q} = 1$, and (*e*) dimensionless flow rate $\tilde{q}$ for $n = 0.7$.

n and large Q, we must determine how the initial thickness difference affects the shear rate difference through n and $\tilde{q}$. We do this by defining two ratios to compare the thicker and thinner films: the shear rate ratio $\hat{\dot{\gamma}} = \tilde{\dot{\gamma}}_1/\tilde{\dot{\gamma}}_2$ and the thickness ratio $\hat{h} = \tilde{h}_1/(\tilde{h}_1 + \tilde{h}_2)$, where $\hat{h} = 0.5$ for symmetric flow. Figure 11(*d*) plots $\hat{\dot{\gamma}}$ against $\hat{h}$, as it depends upon n for $\tilde{q} = 1$, showing that the shear rate ratio increases with asymmetry $\hat{h}$ for all n, and increases faster as n decreases. Thus decreasing n increases the shear rate difference for fixed $\hat{h}$ along with increasing the shear-dependence of μ – the cumulative effect of these produces heavily asymmetric patterns from slightly asymmetric initial conditions, as observed in our experiments. Figure 11(*e*) plots $\hat{\dot{\gamma}}$ against $\hat{h}$, as it depends upon $\tilde{q}$ for $n = 0.7$, showing that $\hat{\dot{\gamma}}$ increases with $\hat{h}$, and increases faster as $\tilde{q}$ increases. Here, an increased flow rate Q leads to a greater shear rate difference in an initially asymmetric film, and increases its ability to amplify into an asymmetric morphology.

References

Armelin, E., Martí, M., Rudé, E., Labanda, J., Llorens, J. & Alemán, C. 2006 A simple model to describe the thixotropic behavior of paints. *Prog. Org. Coat.* **57** (3), 229–235.

Boulogne, F., Fardin, M.-A., Lerouge, S., Pauchard, L. & Giorgiutti-Dauphiné, F. 2013 Suppression of the Rayleigh–Plateau instability on a vertical fibre coated with wormlike micelle solutions. *Soft Matt.* **9** (32), 7787–7796.

BOULOGNE, F., PAUCHARD, L. & GIORGIUTTI-DAUPHINÉ, F. 2012 Instability and morphology of polymer solutions coating a fibre. *J. Fluid Mech.* **704**, 232–250.

BRASSE, G., RESTOIN, C., SOULE, D. & BLONDY, J.-M. 2011 Rheology study of silica–zirconia sols for elaboration of silica–zirconia nanostructured optical fibers by inverse dip coating. *J. Phys. Chem.* C **115** (1), 248–252.

BÜHNE, S., WOOCKER, A. & LINZMAIER, A. 2009 Getting the best effect pigment orientation. *Eur. Coat. J.* **9**, 28–33.

CARROLL, B.J. 1986 Equilibrium conformations of liquid drops on thin cylinders under forces of capillarity. A theory for the roll-up process. *Langmuir* **2** (2), 248–250.

CARROLL, B.J. 1984 The equilibrium of liquid drops on smooth and rough circular cylinders. *J. Colloid Interface Sci.* **97** (1), 195–200.

CHANG, H.-C. & DEMEKHIN, E.A. 1999 Mechanism for drop formation on a coated vertical fibre. *J. Fluid Mech.* **380**, 233–255.

CHINJU, H., UCHIYAMA, K. & MORI, Y.H. 2000 'String-of-beads' flow of liquids on vertical wires for gas absorption. *AIChE J.* **46** (5), 937–945.

CHOU, T.-H., HONG, S.-J., LIANG, Y.-E., TSAO, H.-K. & SHENG, Y.-J. 2011 Equilibrium phase diagram of drop-on-fiber: coexistent states and gravity effect. *Langmuir* **27** (7), 3685–3692.

CRASTER, R.V. & MATAR, O.K. 2006 On viscous beads flowing down a vertical fibre. *J. Fluid Mech.* **553**, 85–105.

DACUS, M., RAIHAN, M.K., BAGHDADY, M., GABBARD, C., WU, S., BOSTWICK, J.B., SONG, Y. & XUAN, X. 2022 Surfactant effects on microfluidic extensional flow of water and polymer solutions. *Phys. Fluids* **34** (3), 032006.

DUPRAT, C., GIORGIUTTI-DAUPHINÉ, F., TSELUIKO, D., SAPRYKIN, S. & KALLIADASIS, S. 2009*a* Liquid film coating a fiber as a model system for the formation of bound states in active dispersive-dissipative nonlinear media. *Phys. Rev. Lett.* **103** (23), 234501.

DUPRAT, C., RUYER-QUIL, C. & GIORGIUTTI-DAUPHINÉ, F. 2009*b* Spatial evolution of a film flowing down a fiber. *Phys. Fluids* **21** (4), 042109.

DUPRAT, C., RUYER-QUIL, C., KALLIADASIS, S. & GIORGIUTTI-DAUPHINÉ, F. 2007 Absolute and convective instabilities of a viscous film flowing down a vertical fiber. *Phys. Rev. Lett.* **98** (24), 244502.

DUPRAT, C., TSELUIKO, D., SAPRYKIN, S., KALLIADASIS, S. & GIORGIUTTI-DAUPHINÉ, F. 2011 Wave interactions on a viscous film coating a vertical fibre: formation of bound states. *Chem. Engng Process.* **50** (5–6), 519–524.

EBRAHIMI, A., NARANJANI, B., MILANI, S. & JAVAN, F.D. 2017 Laminar convective heat transfer of shear-thinning liquids in rectangular channels with longitudinal vortex generators. *Chem. Engng Sci.* **173**, 264–274.

EGHBALI, S., KEISER, L., BOUJO, E. & GALLAIRE, F. 2022 Whirling instability of an eccentric coated fibre. *J. Fluid Mech.* **952**, A33.

GABBARD, C.T. & BOSTWICK, J.B. 2021*a* Asymmetric instability in thin-film flow down a fiber. *Phys. Rev. Fluids* **6** (3), 034005.

GABBARD, C.T. & BOSTWICK, J.B. 2021*b* Scaling analysis of the Plateau–Rayleigh instability in thin film flow down a fiber. *Exp. Fluids* **62**, 141.

GILET, T., TERWAGNE, D. & VANDEWALLE, N. 2009 Digital microfluidics on a wire. *Appl. Phys. Lett.* **95** (1), 014106.

GINGRICH, W.K., CHO, Y.I. & SHYY, W. 1992 Effects of shear thinning on laminar heat transfer behavior in a rectangular duct. *Intl J. Heat Mass Transfer* **35** (11), 2823–2836.

GRÜNIG, J., LYAGIN, E., HORN, S., SKALE, T. & KRAUME, M. 2012 Mass transfer characteristics of liquid films flowing down a vertical wire in a counter current gas flow. *Chem. Engng Sci.* **69** (1), 329–339.

HAEFNER, S., BENZAQUEN, M., BÄUMCHEN, O., SALEZ, T., PETERS, R., MCGRAW, J.D., JACOBS, K., RAPHAËL, E. & DALNOKI-VERESS, K. 2015 Influence of slip on the Plateau–Rayleigh instability on a fibre. *Nat. Commun.* **6**, 7409.

HALPERN, D. & WEI, H.-H. 2017 Slip-enhanced drop formation in a liquid falling down a vertical fibre. *J. Fluid Mech.* **820**, 42–60.

HAWARD, S.J., HOPKINS, C.C. & SHEN, A.Q. 2020 Asymmetric flow of polymer solutions around microfluidic cylinders: interaction between shear-thinning and viscoelasticity. *J. Non-Newtonian Fluid Mech.* **278**, 104250.

HOSSEINI, S.M., ALIZADEH, R., FATEHIFAR, E. & ALIZADEHDAKHEL, A. 2014 Simulation of gas absorption into string-of-beads liquid flow with chemical reaction. *Heat Mass Transfer* **50** (10), 1393–1403.

JI, H., FALCON, C., SADEGHPOUR, A., ZENG, Z., JU, Y.S. & BERTOZZI, A.L. 2019 Dynamics of thin liquid films on vertical cylindrical fibres. *J. Fluid Mech.* **865**, 303–327.

JI, H., FALCON, C., SEDIGHI, E., SADEGHPOUR, A., JU, Y.S. & BERTOZZI, A.L. 2021 Thermally-driven coalescence in thin liquid film flowing down a fibre. *J. Fluid Mech.* **916**, A19.

JI, H., SADEGHPOUR, A., JU, Y.S. & BERTOZZI, A.L. 2020 Modelling film flows down a fibre influenced by nozzle geometry. *J. Fluid Mech.* **901**, R6.

KALLIADASIS, S. & CHANG, H.-C. 1994 Drop formation during coating of vertical fibres. *J. Fluid Mech.* **261**, 135–168.

KHANUM, S. & TIWARI, N. 2020 Gravity-driven thermoviscous liquid film down a heated or cooled vertical cylinder. *Phys. Rev. Fluids* **5** (9), 094005.

KLIAKHANDLER, I.L., DAVIS, S.H. & BANKOFF, S.G. 2001 Viscous beads on vertical fibre. *J. Fluid Mech.* **429**, 381–390.

LABBÉ, R. & DUPRAT, C. 2019 Capturing aerosol droplets with fibers. *Soft Matt.* **15** (35), 6946–6951.

LIN, X., SCHMELTER, D. & HINTZE-BRUENING, H. 2021 High solid waterborne automotive base coat: beyond shear thinning. *Prog. Org. Coat.* **160**, 106530.

MCHALE, G. & NEWTON, M.I. 2002 Global geometry and the equilibrium shapes of liquid drops on fibers. *Colloids Surf. (*A*)* **206** (1–3), 79–86.

MCHALE, G., NEWTON, M.I. & CARROLL, B.J. 2001 The shape and stability of small liquid drops on fibers. *Oil Gas Sci. Technol.* **56** (1), 47–54.

MONCUQUET, A., MITRANESCU, A., MARCHAND, O.C., RAMANANARIVO, S. & DUPRAT, C. 2022 Collecting fog with vertical fibres: combined laboratory and in-situ study. *Atmos. Res.* **277**, 106312.

NGUYEN, L.T., BAI, Z., ZHU, J., GAO, C., LIU, X., WAGAYE, B.T., LI, J., ZHANG, B. & GUO, J. 2021 Three-dimensional multilayer vertical filament meshes for enhancing efficiency in fog water harvesting. *ACS Omega* **6** (5), 3910–3920.

PRADAS, M., TSELUIKO, D., RUYER-QUIL, C. & KALLIADASIS, S. 2014 Pulse dynamics in a power-law falling film. *J. Fluid Mech.* **747**, 460–480.

QUÉRÉ, D. 1999 Fluid coating on a fiber. *Annu. Rev. Fluid Mech.* **31** (1), 347–384.

RUYER-QUIL, C., TREVELYAN, S.P.M.J., GIORGIUTTI-DAUPHINÉ, F., DUPRAT, C. & KALLIADASIS, S. 2009 Film flows down a fiber: modeling and influence of streamwise viscous diffusion. *Eur. Phys.* J.*: Spec. Top.* **166** (1), 89–92.

SADEGHPOUR, A., OROUMIYEH, F., ZHU, Y., KO, D.D., JI, H., BERTOZZI, A.L. & JU, Y.S. 2021 Experimental study of a string-based counterflow wet electrostatic precipitator for collection of fine and ultrafine particles. *J. Air Waste Manage. Assoc.* **71** (7), 851–865.

SADEGHPOUR, A., ZENG, Z., JI, H., DEHDARI EBRAHIMI, N., BERTOZZI, A.L. & JU, Y.S. 2019 Water vapor capturing using an array of traveling liquid beads for desalination and water treatment. *Sci. Adv.* **5** (4), eaav7662.

SADEGHPOUR, A., ZENG, Z. & JU, Y.S. 2017 Effects of nozzle geometry on the fluid dynamics of thin liquid films flowing down vertical strings in the Rayleigh–Plateau regime. *Langmuir* **33** (25), 6292–6299.

SHEN, A.Q., GLEASON, B., MCKINLEY, G.H. & STONE, H.A. 2002 Fiber coating with surfactant solutions. *Phys. Fluids* **14** (11), 4055–4068.

SMOLKA, L.B., NORTH, J. & GUERRA, B.K. 2008 Dynamics of free surface perturbations along an annular viscous film. *Phys. Rev.* E **77** (3), 036301.

TADMOR, Z. & BIRD, R.B. 1974 Rheological analysis of stabilizing forces in wire-coating dies. *Polym. Engng Sci.* **14** (2), 124–136.

TANG, Y., HU, X., ZHANG, X., GUO, D., ZHANG, J. & KONG, F. 2016 Chitosan/titanium dioxide nanocomposite coatings: rheological behavior and surface application to cellulosic paper. *Carbohyd. Polym.* **151**, 752–759.

UCHIYAMA, K., MIGITA, H., OHMURA, R. & MORI, Y.H. 2003 Gas absorption into 'string-of-beads' liquid flow with chemical reaction: application to carbon dioxide separation. *Intl J. Heat Mass Transfer* **46** (3), 457–468.

WYATT, N.B. & LIBERATORE, M.W. 2009 Rheology and viscosity scaling of the polyelectrolyte xanthan gum. *J. Appl. Polym. Sci.* **114** (6), 4076–4084.

XIE, Q., LIU, R., WANG, X. & CHEN, X. 2021 Investigation of flow dynamics of thin viscous films down differently shaped fibers. *Appl. Phys. Lett.* **119** (20), 201601.

YANG, H.Q. 1992 Asymmetric instability of a liquid jet. *Phys. Fluids* A **4** (4), 681–689.

ZENG, Z., SADEGHPOUR, A. & JU, Y.S. 2018 Thermohydraulic characteristics of a multi-string direct-contact heat exchanger. *Intl J. Heat Mass Transfer* **126**, 536–544.

ZENG, Z., SADEGHPOUR, A., WARRIER, G. & JU, Y.S. 2017 Experimental study of heat transfer between thin liquid films flowing down a vertical string in the Rayleigh–Plateau instability regime and a counterflowing gas stream. *Intl J. Heat Mass Transfer* **108**, 830–840.